Whistler turbulence: Particle-in-cell simulations

Shinji Saito*, S. Peter Gary, and Hui Li

Los Alamos National Laboratory

Los Alamos, NM 87545

Yasuhito Narita

Institute of Geophysics and Extraterrestrial Physics

Braunschweig, Germany

15 September 2008

Abstract

Two dimensional electromagnetic particle-in-cell simulations in a magnetized, homogeneous, collisionless electron-proton plasma demonstrate the forward cascade of whistler turbulence. The simulations represent decaying turbulence, in which an initial, narrowband spectrum of fluctuations at wavenumbers $kc/\omega_e \simeq 0.1$ cascades toward increased damping at $kc/\omega_e \simeq 1.0$, where c/ω_e is the electron inertial length. The turbulence displays magnetic energy spectra that are relatively steep functions of wavenumber and are anisotropic with more energy in directions relatively perpendicular to the background magnetic field $\mathbf{B}_o = \hat{\mathbf{x}} B_o$ than at the same wavenumbers parallel to $\mathbf{B}_o$. In the weak turbulence regime, the primary new results of the simulations are: 1) Magnetic spectra of the cascading fluctuations become more anisotropic with increasing fluctuation energy; 2) the wavevector dependence of the three magnetic energy ratios, $|\delta B_j|^2/|\delta \mathbf{B}|^2$ with $j = x, y, z$, show good agreement with linear dispersion theory for whistler fluctuations; 3) the magnetic compressibility summed over the cascading modes satisfies $0.3 \lesssim |\delta B_x|^2/|\delta \mathbf{B}|^2 \lesssim 0.6$; and 4) the turbulence heats electrons in directions both parallel and perpendicular to $\mathbf{B}_o$, with stronger heating in the parallel direction.

I. INTRODUCTION

Solar wind measurements yield fluctuating magnetic energy spectra which usually are power law in the observed frequency f. The spectral indices are frequently measured to be about $-5/3$ [1,2] at $f \lesssim 0.1$ Hz. Kolmogorov theory predicts $|\delta \mathbf{v}|^2 \propto k^{-5/3}$ in isotropic neutral fluid turbulence. Because of this power-law similarity, low frequency magnetohydrodynamic (MHD) turbulence in the solar wind has been called the "inertial

* Current address: STE Laboratory, Nagoya University, Nagoya, Aichi 464-8601 Japan

range". However, in contrast to Kolmogorov turbulence, both solar wind observations [3,4] and numerical computations [5,6] show MHD turbulence to be strongly anisotropic.

In the range 0.2 Hz $\lesssim f \lesssim$ 0.5 Hz, solar wind measurements near 1 AU often show a spectral breakpoint, a distinct change to power-law spectra that are steeper than those of the inertial range [1,4,7]. Such high-frequency spectra are sometimes called the "dissipation range," again by analogy with neutral fluid turbulence. However, theoretical models predict that either Landau or cyclotron damping should lead to spectra with a strong cutoff rather than to the observed power law behavior [8]. The more likely explanation for these steeper power-law spectra is that the fluctuations are weakly damped dispersive waves [9], and recent observations [7] support this view. The character of such spectra is not well understood, so we use the term "short-wavelength turbulence" to denote this regime.

Several different scenarios have been put forward to explain the properties of short-wavelength turbulence. One possibility is that the plasma physics of this regime is associated with fundamentally nonlinear modes and nonlinear processes [7,10]. An alternate viewpoint is based upon the assumption of weak turbulence, which uses linear dispersion theory to describe the real frequencies and damping rates of the fluctuations.

Within the weak turbulence approximation, there is a current controversy about the identity of the principal constituent of short-wavelength turbulence in the solar wind. In one scenario [11], compressive modes are regarded as damped in the collisionless inertial range, but long-wavelength Alfvénic turbulence cascades down to the scale of the ion gyroradius, where the fluctuations are subject to ion Landau damping and the spectral breakpoint ensues. The remaining fluctuation energy continues to cascade to shorter wavelengths as kinetic Alfvén waves, relatively incompressible modes which propagate with wavevector $\mathbf{k}$ strongly oblique to the background magnetic field, $\mathbf{B}_o$, and at frequencies below Ω_p, the proton cyclotron frequency. These fluctuations finally are completely damped via the electron Landau resonance at wavelengths of the order of the electron gyroradius. Both observational [4, 12] and computational [13] arguments have been advanced in favor of this interpretation.

In a second scenario [9], cascading left-hand polarized Alfvénic fluctuations are subject to proton cyclotron damping at $k_\parallel c/\omega_p \gtrsim 1$ [14,15]. Here c/ω_p is the proton inertial length and $\parallel$ and $\perp$ denote directions respectively parallel and perpendicular to $\mathbf{B}_o$. In this scenario, the spectral breakpoint corresponds approximately to $kc/\omega_p \simeq 1$ [16,17]; in agreement with the first scenario, the only Alfvénic modes which may contribute to turbulence at shorter wavelengths are kinetic Alfvén waves at $k_\perp$ substantially greater than $k_\parallel$. This scenario differs from the first, however, in that it admits right-hand polarized magnetosonic fluctuations at quasi-parallel propagation as weakly damped for $\beta_p \lesssim 1$ and $kc/\omega_p \lesssim 1$ [9]. Thus these fluctuations also contribute to the inertial range cascade, Because they are not damped at the ion inertial wavelengths, these fluctuations cascade to $kc/\omega_p \gtrsim 1$

where they become dispersive whistlers [18] with steeper power-law wavenumber spectra [1]. This cascading whistler turbulence ultimately dissipates via electron cyclotron and/or Landau damping at $k\lambda_e \sim 1$, where λ_e is c/ω_e, the electron inertial length.

In the framework of the second scenario, we here use particle-in-cell simulations to examine properties of whistler turbulence. Turbulent-like whistler fluctuations are observed in the solar wind [19, 20], and are a likely source of electron scattering in that medium [21-23], but the physics of such turbulence is not fully understood. Electron magnetohydrodynamic (EMHD) models, in which the ions are assumed to be stationary and electrons are represented as a fluid, yield energy spectra $|\delta\mathbf{B}|^2 \sim k^{-7/3}$ in both two-dimensional [24, 25] and three-dimensional [26, 27] simulations over $k\lambda_e < 1$. Furthermore, such models show that whistler turbulence in magnetized plasmas is anisotropic, evolving to a state in which there is more magnetic fluctuation energy at wavenumbers relatively perpendicular to $\mathbf{B}_o$ than at parallel wavenumbers [25, 27]. EMHD theory [28] also predicts the development of a similar anisotropy in whistler turbulence.

However, a kinetic approach is necessary to provide a complete description of whistler turbulence in collisionless plasmas. Particle-in-cell simulations, which represent both electrons and ions as super-particles, capture not only the wave-wave interactions represented by fluid descriptions such as EMHD, but also the wave-particle interactions such as Landau and cyclotron damping which are the ultimate dissipation mechanisms of cascading whistlers. The limitations of the PIC simulation method are not due to any analytic model approximations, but rather are due to limits on particle number, cell size, and computing time due to constrained computing resources. Reference 29 described the first particle-in-cell simulation to demonstrate cascading whistler turbulence. In this computation an initial narrowband spectrum of relatively long wavelength whistlers was prescribed, and the subsequent response of the fields and plasma was computed to $|\Omega_e|t = 447$. The resulting turbulent spectrum was anisotropic in the same sense as predicted by EMHD models, but also showed that damping of the turbulence led to heating of the electron velocity distribution in the directions parallel and antiparallel to $\mathbf{B}_o$. This manuscript elaborates upon that initial computation, describing results from an ensemble of whistler turbulence simulations which have been run to longer times, specifically, $|\Omega_e|t = 2011$.

Our simulations show that whistler turbulence exhibits a significant magnetic compressibility, which we define as

$$C_{\parallel}(\mathbf{k}) \equiv \frac{|\delta B_{\parallel}(\mathbf{k})|^2}{|\delta\mathbf{B}(\mathbf{k})|^2} \tag{1}$$

Recent measurements demonstrate that short-wavelength turbulence has greater magnetic compressibility than inertial range fluctuations [7, 30, 31]. Oblique whistlers have substantially larger magnetic compressibilities than kinetic Alfvén waves, implying that the former mode is the more likely constituent of short wavelength turbulence in the solar wind.

II. SIMULATION MODEL AND PARAMETERS

As in Reference 29, we used a 2D3V, fully relativistic, collisionless electromagnetic particle-in-cell code modified from the TRISTAN code [32]. Here "2D" and "3V" mean that we consider plasma behavior in two spatial dimensions (x, y) but full three-dimensional velocity space (v_x, v_y, v_z). This code solves Faraday's and Ampere's equations for the electric and the magnetic field, and solves the equations of motion for all electron and proton super-particles. The electric current is obtained from the motion of the charged particles and fed back into Ampere's equation. We use an electron-proton plasma with periodic boundary conditions for the super-particles and the electromagnetic fields on both x and y boundaries. The number of grids for our simulations is $L_x \times L_y = 1024 \times 1024$. The electron-proton pairs are uniformly distributed with the number of super-particles per cell $N_e = N_p = 64$. The subscripts "e" and "p" represent electron and proton species. The time step δt for our computations is $0.05/\omega_e$ where ω_e is the electron plasma frequency and the grid spacing Δ is $0.1\lambda_e$. Here $\mathbf{B}_o = \hat{\mathbf{x}} B_o$. The initial physical dimensionless parameters are the same as in Reference 29: the mass ratio $m_p/m_e = 1836$, the temperature ratio $T_p/T_e = 1$, the ratio of the electron plasma and the electron cyclotron frequency $\omega_e/|\Omega_e| = 2.236$, and the electron plasma beta $\beta_e = 0.1$. We assume a relatively hot plasma with electron thermal speed $v_e/c = 0.1$, where c is the speed of light.

We impose 42 right-hand polarized whistler waves at $t = 0$. Initial wavenumbers parallel to $\mathbf{B_o}$ are $k_x\lambda_e = \pm 0.0613$, ± 0.1227, and ± 0.184, whereas perpendicular wavenumbers k_y are the six values for k_x and $k_y = 0$. The frequencies are derived from the linear dispersion relation for magnetosonic-whistler fluctuations in a collisionless plasma with the same parameters as shown above. Each wave has an equal fluctuating magnetic energy at $t = 0$. Given the initial magnetic fluctuations $\delta\mathbf{B}_n$, the initial $\delta\mathbf{E}_n$ and $\delta\mathbf{J}_n$ satisfy Faraday's and Ampere's equations, where the subscript "n" is a mode number from 1 to 42 for the initial fluctuations. We neglect the electrostatic and particle density contributions to the initial fluctuations. We argue that neglecting these small contributions is not a concern because the calculations should adjust the initial fluctuations to self-consistent fluctuations within a few electron plasma periods. We define θ, the angle of mode propagation, by $\mathbf{k}\cdot\mathbf{B}_o = kB_o \cos(\theta)$.

III. SIMULATION RESULTS

We have done three simulations in which the only initial parameter which is varied is the initial fluctuation energy $\epsilon_B \equiv \sum_{n=1}^{42} |\delta\mathbf{B}_n(t = 0)|^2/B_o^2$, where $|\delta\mathbf{B}_n|^2 = \sum_{j=x,y,z} |\delta B_{j,n}|^2$. The three simulations, denoted as Run I, Run II, and Run III, have $\epsilon_B = 0.1$, 0.05, and 0.02, respectively. This section shows results from these three simulations, placing emphasis on the properties of the wavenumber spectra, the spectral

anisotropy, and the magnetic compressibility in the cascaded turbulence. We also analyze electron scattering by the turbulent fluctuations.

Magnetic energy spectra. Figure 1 shows the magnetic fluctuation energy spectra $|\delta\mathbf{B}(k_x,k_y)|^2/B_o^2$ at $|\Omega_e|t = 2011$ for all three simulations. One-dimensional reduced spectra labeled as "a" are obtained from the full two-dimensional spectra labeled as "b" by integrating on the other direction; e.g., $|\delta\mathbf{B}(k_x)|^2 \equiv \Sigma_{k_y}|\delta\mathbf{B}(k_x,k_y)|^2$. The two dimensional spectra are plotted as contours in (k_x,k_y) space. Magnetic fluctuation energy transfer appears in wavenumbers $|k_x\lambda_e| > 0.184$ and $|k_y\lambda_e| > 0.184$. In Run I, as in Reference 29, the cascaded magnetic fluctuations approximately satisfy a power law dependence as a function of both k_x and k_y; that is, in wavenumbers parallel and perpendicular to $\mathbf{B}_o$, respectively. At smaller ϵ_B, the spectra do not show a clear power law dependence.

We define α_x and α_y by $|\delta\mathbf{B}(k_j)|^2 = Ck_j^{-\alpha_j}$ for $j = x, y$. Then at the end of Run I, $\alpha_y = 4.5$ and $\alpha_x = 9.0$. Plots of reduced spectra at various times during the simulation (not shown here) demonstrate that the perpendicular spectrum does not undergo significant change (e.g., for the same initial parameters, $\alpha_y = 4.6$ at $|\Omega_e|t = 447.0$ in Reference 29). However, $|\mathbf{B}(k_x)|^2$ becomes steeper with time increasing over $400 \lesssim |\Omega_e|t \lesssim 2000$ ($\alpha_x = 6.8$ at $|\Omega_e|t = 447.0$ in Reference 29), suggesting that electron cyclotron damping is dissipating fluctuations at relatively large values of k_x.

Spectral anisotropies. The two-dimensional spectra in all three simulations are clearly anisotropic with more energy at wavenumbers relatively perpendicular to $\mathbf{B}_o$ than at parallel wavenumbers. To quantify this anisotropy, we follow Reference 5 and define the spectral anisotropy angle θ_B by

$$\tan^2\theta_B \equiv \frac{\Sigma_k k_y^2|\delta\mathbf{B}(k_x,k_y)|^2}{\Sigma_k k_x^2|\delta\mathbf{B}(k_x,k_y)|^2} \tag{2}$$

An isotropic spectrum corresponds to $\tan^2\theta_B = 1.0$. The wavenumber range of the summations is over the cascaded fluctuations, $0.30 \le |k\lambda_e| \le 3.0$.

Figure 2 shows (a) the total magnetic energy density and (b) the spectral anisotropy for the cascaded fluctuations as functions of time. The cascaded magnetic energy is larger at larger ϵ_B. This is because the energy cascade rate is a function of fluctuation amplitude. Both the magnetic energy and the spectral anisotropy increase at early times and decrease at late times in all three simulations.

Figure 3 illustrates $\tan^2\theta_B$ as a function of the instantaneous cascading magnetic energy density. In each simulation the early-time points correspond to relatively isotropic, relatively weak turbulence. As more energy cascades into the range $k\lambda_e \ge 0.3$, there are increases in both the energy density and the spectral anisotropy (as in Figure 2), but at later times both quantities gradually decrease. Even though the anisotropy is relatively scattered in Figure 3 at the larger fluctuating magnetic energies of Run I, it is evident that there is a positive correlation between the two. We conclude that, in the limit of weak

turbulence ($|\delta\mathbf{B}|^2/B_o^2 << 1$), the spectral anisotropy of whistler turbulence increases with the local fluctuation energy density.

Magnetic compressibilities. Magnetic energy ratios $|\delta B_j|^2/|\delta\mathbf{B}|^2$ for $j = x, y, z$ can be directly calculated from linear dispersion theory, so that they may be useful in the identification of constituent modes in weak turbulence. Linear dispersion theory for homogeneous, Maxwellian plasmas typically assumes a two-dimensional wavevector [e.g. Reference 33], corresponding directly to the geometry of our two-dimensional simulations. Note that the magnetic energy ratio $|\delta B_x|^2/|\delta\mathbf{B}|^2$ is equal to the magnetic compressibility defined by Equation (1).

Figure 4 compares simulation results averaged over all times for Run I and linear theory predictions for the three magnetic energy ratios of whistler fluctuations at $kc/\omega_e \simeq 0.3$, 0.5 and 1.0. Figure 4 shows that the simulation results agree with linear theory for whistler fluctuations for most values of θ and all three wavenumbers. Magnetic ratios averaged over Runs II and III (not shown here) also agree with the linear theory predictions, so that the cascaded magnetic fluctuations may be identified as whistlers. These results show not only that the magnetic compressibility of whistler fluctuations increases as propagation becomes more oblique to $\mathbf{B}_o$, but also suggests that linear theory provides a useful description of these small-amplitude, short-wavelength fluctuations.

We have also computed the total $C_\parallel$, that is, the magnetic compressibility summed over all the cascading wavenumbers. We find that, for all three runs, there are no discernable trends of this quantity as a function of either time or $|\delta\mathbf{B}|^2/B_o^2$, with the parametric range $0.3 \lesssim C_\parallel \lesssim 0.6$.

Electron scattering. Figure 5 shows time histories of (a) the parallel electron kinetic energy $E_{\parallel,kin} = \sum m_e v_{x,e}^2/2$, (b) the perpendicular electron kinetic energy $E_{\perp,kin} = \sum m_e(v_{y,e}^2 + v_{z,e}^2)/4$, and (c) the ratio of $E_{\perp,kin}$ and $E_{\parallel,kin}$. These kinetic energies are summed over all electrons, and are normalized to the background magnetic field energy integrated over the simulation box. The parallel kinetic energies increase more rapidly at early times; however, their growth tends to be weak at late times. On the other hand, the perpendicular kinetic energies increase relatively uniformly in time. Overall, the electrons gain more energy at larger initial fluctuation energies. The ratio of the perpendicular and parallel electron kinetic energy shows that larger initial fluctuating magnetic energies provide greater energy gains of electrons which are preferentially heated in the parallel direction.

Figure 6 illustrates differences between $f_e(v_x, v_y, |\Omega_e|t = 2011)$ and $f_e(v_x, v_y, |\Omega_e|t = 0)$ normalized to $f_e(0,0,0)$ for Run I, Run II, and Run III. All three runs indicate parallel heating of electrons by Landau resonance as in Reference 29. But there is also evidence of perpendicular heating especially at larger initial amplitudes, as shown in Figure 5. Note that at late times, growth of the parallel energy becomes weak whereas the perpendicular

kinetic energy continues to increase. Figure 6 shows contours of color plots approximately correspond to curves of constant kinetic energy ($v_x^2 + v_y^2 \approx$ constant), a likely signature of pitch angle scattering at the electron cyclotron resonance.

IV. INTERPRETATION

The agreement between linear theory and the simulations for the magnetic energy ratios indicates that weak whistler turbulence may well be described as a weakly coupled collection of linear normal modes. In this framework, we offer an interpretation of our simulation results.

An important question is: Is the spectral anisotropy of whistler turbulence in our simulations due to nonlinear cascade processes, or to preferential collisionless damping at parallel propagation? The EMHD model results described earlier do not include collisionless dissipation, and indicate that the perpendicular anisotropy should be due to nonlinear wave-wave interactions. However, electron cyclotron damping preferentially damps fluctuations at parallel propagation and could be an alternate source of this anisotropy.

To address this question, we return to linear dispersion theory [33] and in Figure 7 plot the damping rate for whistler fluctuations in an electron-proton plasma of $\beta_e = 0.10$. Figure 7a plots the damping rate as a function of wavenumber, and illustrates the difference between electron cyclotron damping and electron Landau damping. The former is the only collisionless damping at $\theta = 0^o$, and is essentially zero at $k_\| c/\omega_e \lesssim 0.7$ but has a sudden onset at about $k_\| c/\omega_e = 0.8$. In contrast, electron Landau damping, which arises only at $\theta > 0^o$, has no clear onset, but gradually increases with increasing wavenumber across the full range of wavenumbers in our simulations. Figure 7b shows the damping rate as a function of θ, demonstrating that Landau damping yields the largest value of $|\gamma/\Omega_e|$ in the range $50^o \leq \theta \leq 60^o$.

For our simulations which run to $|\Omega_e|t \simeq 2000$, we assume $\gamma/|\Omega_e|$ = -0.005 which corresponds to appreciable damping. Electron cyclotron damping reaches this level of dissipation at $k_\| c/\omega_e \simeq 0.85$, whereas at $\theta = 60^o$ electron Landau damping attains this magnitude of damping at $k_\perp c/\omega_e \simeq 0.45$. Thus the cascading whistler turbulence in our simulations should reach a strong damping condition at oblique propagation well before it attains dissipation in $k_\|$. This is consistent with the results of Figure 5 and Figure 6, which show that electron heating in $v_\|$ which is associated with the Landau resonance at oblique propagation is stronger than electron scattering toward perpendicular velocities which is due to the cyclotron resonance which is primarily a function of $k_\|$. If damping were the dominant factor in shaping the spectral anisotropy, we would expect an anisotropy opposite to that which results from our simulations. Thus we conclude that the primary factors in shaping the anisotropy of the magnetic fluctuations are the nonlinear wave-wave interactions which drive the spectral cascade.

To interpret our simulation results, we calculate scaling relations using a model similar to those discussed in References 24, 27, and 28. We consider the interaction of whistler wave packets with parallel widths $l_\parallel = 2\pi/k_\parallel$ where the constituent modes each satisfy the approximate whistler dispersion equation $\omega_r \simeq k_\parallel k c^2 |\Omega_e|/\omega_e^2$. The wave packet interaction time τ_w is determined by fluctuation properties at propagation parallel to $\mathbf{B}_o$, so

$$\tau_w \simeq \frac{l_\parallel}{(\partial\omega/\partial k_\parallel)}$$

For an eddy of scale length l the turnover time is $\tau_{eddy} \simeq l/\delta v_e$ where the denominator is the fluctuating electron velocity from the EMHD model. Then

$$\tau_{eddy} \simeq \frac{2\pi}{|\Omega_e|}\frac{\omega_e^2}{k^2c^2}\frac{B_o}{|\delta\mathbf{B}|}$$

Following the usual assumption of weak incoherent interactions between eddies, the time scale for the cascade of turbulent fluctuation energy is

$$\tau_{cascade} \equiv \frac{\tau_{eddy}^2}{\tau_w}$$

For Case I, consider whistlers with $k_\parallel << k_\perp$. Then, as in Eq. (70) of Reference 28,

$$\tau_w(k_\perp) \simeq \frac{2\pi}{|\Omega_e|}\frac{\omega_e^2}{k_\parallel k_\perp c^2}$$

and the perpendicular cascade time is

$$\tau_{cascade}(k_\perp) \simeq \frac{2\pi}{|\Omega_e|}\frac{k_\parallel\omega_e^2}{k_\perp^3 c^2}\frac{B_o^2}{|\delta\mathbf{B}(k_\perp)|^2} \tag{3}$$

In Case II, consider interacting whistler wave packets with $k_\parallel >> k_\perp$. Then

$$\tau_w(k_\parallel) \simeq \frac{\pi}{|\Omega_e|}\frac{\omega_e^2}{k_\parallel^2 c^2}$$

and it follows that the parallel cascade time is

$$\tau_{cascade}(k_\parallel) \simeq \frac{4\pi}{|\Omega_e|}\frac{\omega_e^2}{k_\parallel^2 c^2}\frac{B_o^2}{|\delta\mathbf{B}(k_\parallel)|^2} \tag{4}$$

For the cascading power spectra at $k_y c/\omega_e \geq 0.40$ illustrated in Figure 1, Equations (3) and (4) yield $|\Omega_e|\tau_{cascade} > 10^5$. This is much longer than our simulation times of $|\Omega_e|t \simeq 2000$. The implication is that our simulations are in an intermediate, evolving

state, rather than a late-time quasi-steady condition. This is consistent with the results of Figure 2, which also imply a slow evolution of the turbulence.

We can gain additional insight by comparing Equations (3) and (4). Remembering that $k_\perp >> k_\parallel$ in Case I, we assume that the $k_\perp$ of Case I is the same order as $k_\parallel$ of Case II. Furthermore, from Figure 1, $|\delta\mathbf{B}(k_\perp)|^2 \gtrsim |\delta\mathbf{B}(k_\parallel)|^2$; then it follows that $\tau_{cascade}(k_\parallel) >> \tau_{cascade}(k_\perp)$. Thus our model predicts that the cascade rate of whistler turbulence propagating relatively perpendicular to $\mathbf{B}_o$ should be much faster than the cascade rate at quasi-parallel propagation, consistent with the anisotropies of our simulations. Furthermore, since both cascade rates are proportional to the fluctuating magnetic energy densities, it also follows that the model predictions are consistent with the simulation results of Figure 3 which shows that the anisotropy of the fluctuation spectra increases with increasing $|\delta\mathbf{B}|^2$.

V. CONCLUSIONS

We have carried out particle-in-cell simulations of decaying whistler turbulence undergoing a forward cascade in a magnetized, homogeneous, collisionless plasma. The simulations evolve to turbulence with magnetic spectra that are steeper than in the inertial range and anisotropic with more energy in directions relatively perpendicular to the background magnetic field rather than parallel (Figure 1). The sense of the anisotropy is consistent with that from EMHD simulations in magnetized plasmas [25, 27] and with the anisotropy predicted by EMHD theory [28].

The primary new results of these computations are: (1) the spectral anisotropy increases with increasing fluctuation energy, (2) the magnetic energy ratios for all three components of $\delta\mathbf{B}$ agree well with the predictions of linear dispersion theory, (3) the total magnetic compressibility is relatively large, and (4) the magnetic fluctuations heat electrons in directions both parallel and perpendicular to $\mathbf{B}_o$.

The correlation between fluctuation energies and spectral anisotropies suggests a simple explanation: Increasing turbulence energy more strongly drives the nonlinear processes which lead to the perpendicular cascade. As linear dispersion theory predicts that obliquely propagating whistlers are substantially compressive, and the simulations show that the whistler cascade preferentially excites such oblique modes, it follows that whistler turbulence can be strongly compressive. In the whistler-versus-kinetic-Alfvén controversy, the compressibility of whistler turbulence argues in support of that mode as important in the solar wind, where short-wavelength turbulence is indeed observed to be substantially compressive [7, 30, 31].

Figures 1 and 2 indicate that larger fluctuation energy densities correspond to faster energy cascade rates and smaller values of α_y. This anti-correlation between energy cascade rate and spectral steepness is opposite to the direct correlation between these two quantities

reported by [1]. This may be due to the difference in wavenumber regimes; the observations of Reference [1] correspond to $1.0 \lesssim kc/\omega_p < 10.0$, whereas our simulations span $0.10 < kc/\omega_e \lesssim 1$. Another reason for this apparent discrepancy may be that, as discussed above, our simulations are in a state of gradual evolution, whereas solar wind turbulence may have sufficient time to attain a quasi-steady condition; the scaling relations may be different for dynamic and static systems. Resolution of this apparent difference is a worthy subject of future research.

In our simulations electron kinetic energy preferentially increases in directions parallel rather than perpendicular to $\mathbf{B}_o$ and both parallel and perpendicular heating increase with increasing fluctuation energy (Figure 5). Parallel heating is likely associated with electron Landau damping which arises only for oblique whistler propagation; in contrast, perpendicular heating is more likely due to electron cyclotron damping which is most effective for whistlers at parallel propagation. Because our simulations have shown that whistler turbulence evolves preferentially to oblique propagation, electrons gain more energy in the parallel direction.

In our simulations, $|\delta B_z|^2/|\delta \mathbf{B}|^2$ is relatively independent of both initial fluctuating energy and wavenumber. This may be a property of the two dimensional character of our simulations. Three dimensional particle-in-cell simulations will be necessary to provide a full physical picture of whistler turbulence.

Acknowledgments. We acknowledge useful discussions with Joe Borovsky, and very helpful comments from the referee. This work was performed under the auspices of the U.S. Department of Energy (DOE). It was supported by the Institute of Geophysics and Planetary Physics at Los Alamos, by the Magnetic Turbulence and Kinetic Dissipation Project of the Laboratory Directed Research and Development Program at Los Alamos, by Department of Energy Project No. LA06-GPRB-NEM01, and by the Solar and Heliospheric Physics SR&T Program of the National Aeronautics and Space Administration.

References

1. Smith, C. W., K. Hamilton, B. J. Vasquez, and R. J. Leamon (2006), *Astrophys. J.*, *645*, L85.

2. Podesta, J. J., D. A. Roberts, and M. L. Goldstein (2007), *Astrophys. J.*, *664*, 543.

3. Matthaeus, W. H., M. L. Goldstein, and D. A. Roberts (1990), *J. Geophys. Res.*, *95*, 20,673.

4. Leamon, R. J., C. W. Smith, N. F. Ness, W. H. Matthaeus, and H. K. Wong (1998), *J. Geophys. Res.103*, 4775.

5. Shebalin, J. V., W. H. Matthaeus, and D. Montgomery (1983), *J. Plasma Phys.*, *29*, 525.

6. Matthaeus, W. H., S. Oughton, S. Ghosh, and M. Hossain (1998), *Phys. Rev. Lett.*, *81*, 2056.

7. Alexandrova, O., V. Carbone, P. Veltri, and L. Sorriso-Valvo (2008), *Astrophys. J.*, *674*, 1153.

8. Li, H., S. P. Gary and O. Stawicki (2001), *Geophys. Res. Lett.*, *28*, 1347.

9. Stawicki, O., S. P. Gary, and H. Li (2001), *J. Geophys. Res.*, *106*, 8273.

10. Markovskii, S. A., B. J. Vasquez, and C. W. Smith (2008), *Astrophys. J.*, *675*, 1576.

11. Howes, G. G. (2008), *Phys. Plasmas*, *15*, 055904.

12. Bale, S. D., P. J. Kellogg, F. S. Mozer, T. S. Horbury, and H. Reme (2005), *Phys. Rev. Lett.94*, 215002.

13. Howes, G. G., W. Dorland, S. C. Cowley, G. W. Hammett, E. Quataert, A. A. Schekochihin, and T. Tatsuno (2008), *Phys. Rev. Lett.*, *100*, 065004.

14. Gary, S. P. (1999), *J. Geophys. Res.*, *104*, 6759.

15. Gary, S. P., and J. E. Borovsky (2004), *J. Geophys. Res.*, *109*, A06105, doi:10.1029/2004JA010399.

16. Leamon, R. J., W. H. Matthaeus, C. W. Smith, G. P. Zank, D. J. Mullan, and S. Oughton (2000), *Astrophys. J.*, *537*, 1054.

17. Smith, C. W., D. J. Mullan, N. F. Ness, R. M. Skoug, and J. Steinberg, (2001), *J. Geophys. Res.*, *106*, 18,625.

18. Goldstein, M. L., D. A. Roberts, and C. A. Fitch (1994), *J. Geophys. Res.*, *99*, 11,519.

19. Beinroth, H. J., and F. M. Neubauer (1981), *J. Geophys. Res.86*, 7755.

20. Lengyel-Frey, D., R. A. Hess, R. J. MacDowall, R. G. Stone, N. Lin, A. Balogh, and R. Forsyth (1996), *J. Geophys. Res.*, *101*, 27,555.

21. Vocks, C., C. Salem, R. P. Lin, and G. Mann (2005), *Astrophys. J.*, *627*, 540.

22. Saito, S., and S. P. Gary (2007a), *Geophys. Res. Lett.*, *34*, L01102, doi:10.1029/2007GL028173.

23. Saito, S., and S. P. Gary (2007b), *J. Geophys. Res.*, *112*, A06116, doi:10.1029/-2006JA012216.

24. Biskamp, D., E. Schwartz, and J. F. Drake (1996), *Phys. Rev. Lett.*, *76*, 1264.

25. Dastgeer, S., A. Das, P. Kaw, and P. H. Diamond (2000), *Phys. Plasmas*, *7*, 571.

26. Biskamp, D., E. Schwartz, A. Zeiler, A. Celani, and J. F. Drake (1999), *Phys. Plasmas*, *6*, 751.

27. Cho, J., and A. Lazarian (2004), *Astrophys. J.*, *615*, L41.

28. Galtier, S., and A. Bhattacharjee (2003), *Phys. Plasmas*, *10*, 3065.

29. Gary, S. P., S. Saito, and H. Li (2008), *Geophys. Res. Lett.*, *35*, L02104, doi:10.1029/2007GL032327.

30. Hamilton, K., C. W. Smith, B. J. Vasquez, and R. J. Leamon (2008), *J. Geophys. Res.*, *113*, A01106, doi:10.1029/2007JA012559.

31. Narita, Y., K.-H. Glassmeier, S. P. Gary, M. L. Goldstein, and R. A. Treumann (2008), Analysis of wave number spectra through the terrestrial bow shock, *J. Geophys. Res.*, in press.

32. Buneman, O. (1993), Computer space plasma physics, in *Simulation Techniques and Software*, edited by H. Matsumoto and Y. Omura, P. 67, Terra Sci., Tokyo.

33. Gary, S. P. (1993), *Theory of Space Plasma Microinstabilities*, Cambridge University Press, New York.

Figure Captions

Figure 1. (Color online) Magnetic fluctuation energy spectra $|\delta\mathbf{B}(\mathbf{k})|^2/B_o^2$ at $|\Omega_e|t = 2011$ for all three simulations labeled as I, II, and III. The reduced energy spectra labeled as "a" are calculated from the two-dimensional energy spectra labeled as "b" by integrating on the other direction. Red lines (lower curves in the cascade regime) and blue lines (upper curves in the cascade regime) with solid circles in the reduced energy spectra correspond to $j = x$ and $j = y$, respectively.

Figure 2. (Color online) Time histories of quantities summed over the cascading wavenumber range $0.3 \leq |kc/\omega_e| \leq 3.0$ for Run I (upper red line), Run II (middle blue line), and Run III (bottom green line). (a) Total magnetic fluctuation energy and (b) spectral anisotropy $\tan^2\theta_B$.

Figure 3. (Color online) Spectral anisotropy as a function of the instantaneous $|\delta\mathbf{B}|^2/B_o^2$ for Run I (red), Run II (blue), and Run III (green). For the black-and-white version of the figure, the points for Run I correspond to $10^{-3} < |\delta\mathbf{B}|^2/B_o^2$, the points for Run II correspond to $2\times10^{-4} < |\delta\mathbf{B}|^2/B_o^2 < 10^{-3}$, and the points for Run III correspond to $|\delta\mathbf{B}|^2/B_o^2 < 2\times10^{-4}$. Each point corresponds to a summation over the cascading wavenumber range $0.3 \leq |kc/\omega_e| \leq 3.0$.

Figure 4. (Color online) Three magnetic energy ratios as functions of θ for three ranges of $|kc/\omega_e|$ as labeled. Here the green or upper points indicate $|\delta B_z|^2/|\delta\mathbf{B}|^2$, the blue or decreasing points indicate $|\delta B_y|^2/|\delta\mathbf{B}|^2$, and the red or increasing points indicate $|\delta B_x|^2/|\delta\mathbf{B}|^2$, the magnetic compressibility. Run I and linear theory results are shown by open circles and dashed lines, respectively. The simulation results are averaged over the whole time of the computation.

Figure 5. (Color online) Time histories of (a) parallel electron kinetic energy $E_{\parallel,kin}$, (b) perpendicular electron kinetic energy $E_{\perp,kin}$, and (c) ratio of the perpendicular and the parallel electron kinetic energy. These energies are normalized to the background magnetic

field energy $E_{o,B}$. Here red denotes results from Run I, blue denotes results from Run II, and green denotes results from Run III. In black-and-white, Run I curves are uppermost in panels (a) and (b), and lowermost in panel (c); Run II curves are in the middle, and Run III curves are lowermost in panels (a) and (b) and uppermost in panel (c).

Figure 6. (Color online) Differences between the late-time and initial electron velocity distributions, that is, $[f_e(v_x, v_y, |\Omega_e|t = 2011) - f_e(v_x, v_y, |\Omega_e|t = 0)]/f_e(v_x = 0, v_y = 0, |\Omega_e|t = 0)$ for Run I (top), Run II (middle), and Run III (bottom).

Figure 7. Linear dispersion theory for whistler fluctuations in a homogeneous, collisionless, electron-proton plasma with $\beta_e = 0.10$. (a) Whistler damping rates as functions of wavenumber for four angles of propagation as labeled. (b) Whistler damping rates as functions of propagation angle for five values of wavenumber as labeled.

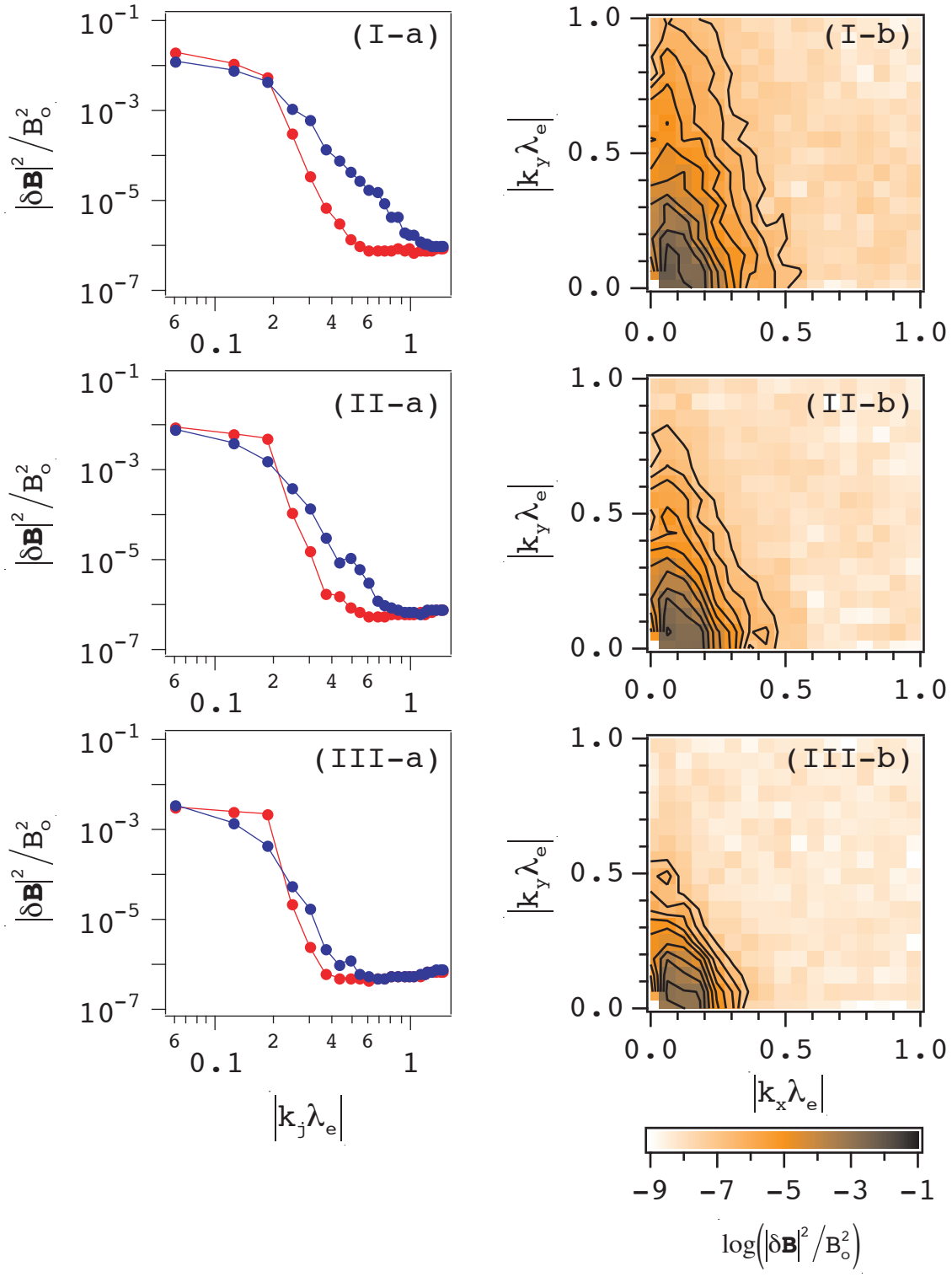
(I-a)
(II-a)
(III-a)
(I-b)
(II-b)
(III-b)
$|\delta \mathbf{B}|^2/B_o^2$
10^{-1}
10^{-3}
10^{-5}
10^{-7}
6
2
4
6
0.1
1
$|k_j \lambda_e|$
$|k_y \lambda_e|$
1.0
0.5
0.0
$|k_x \lambda_e|$
−9
−7
−5
−3
−1
$\log\left(|\delta \mathbf{B}|^2/B_o^2\right)$

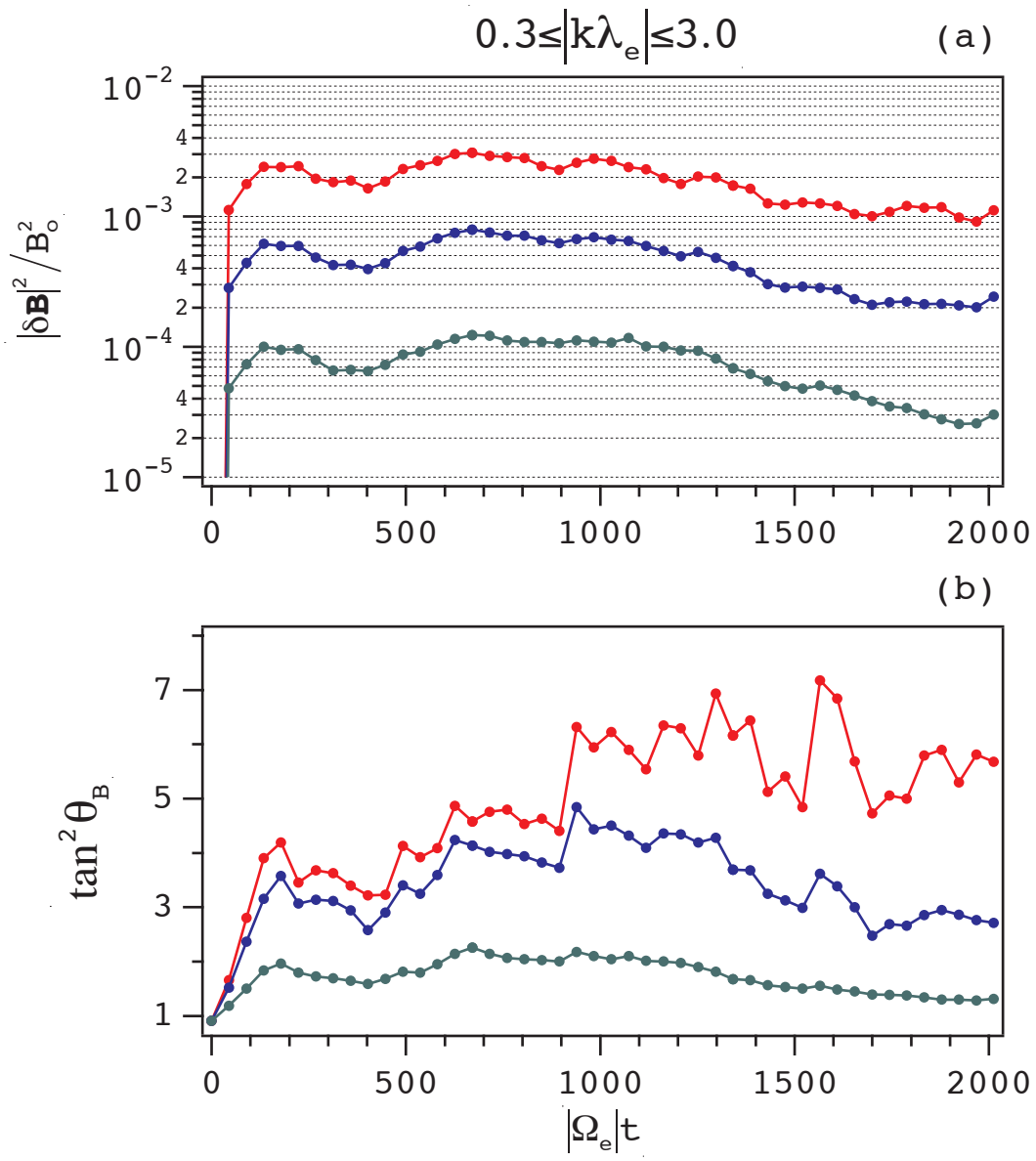
0.3≤|kλe|≤3.0
(a)
10^-2
10^-3
10^-4
10^-5
|δB|^2/B_o^2
0
500
1000
1500
2000
(b)
tan^2θ_B
7
5
3
1
0
500
1000
1500
2000
|Ωe|t

Figure 2

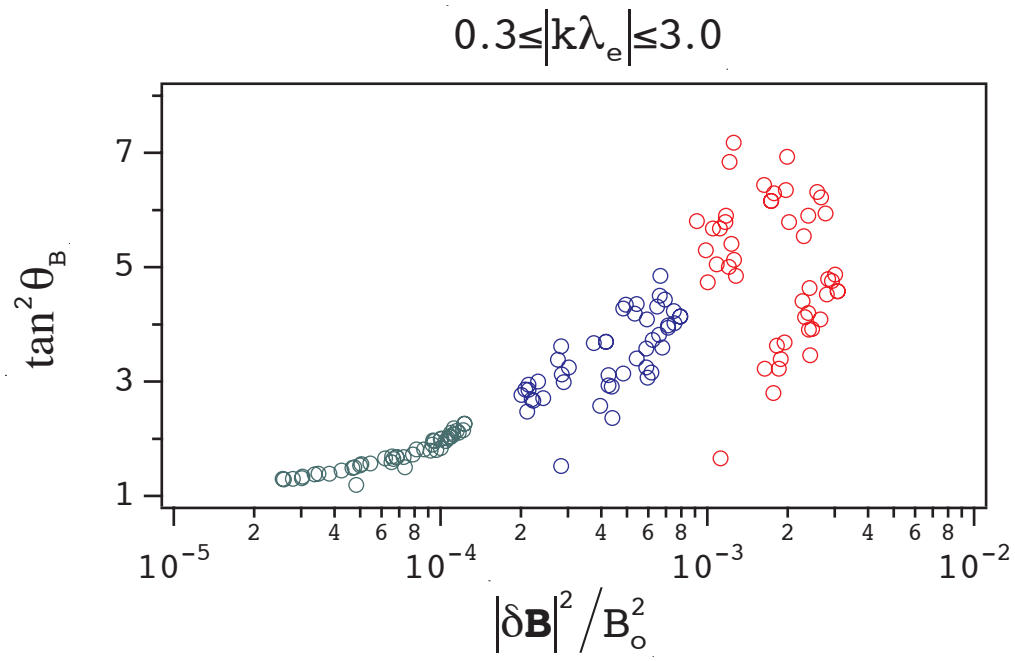

Figure 3

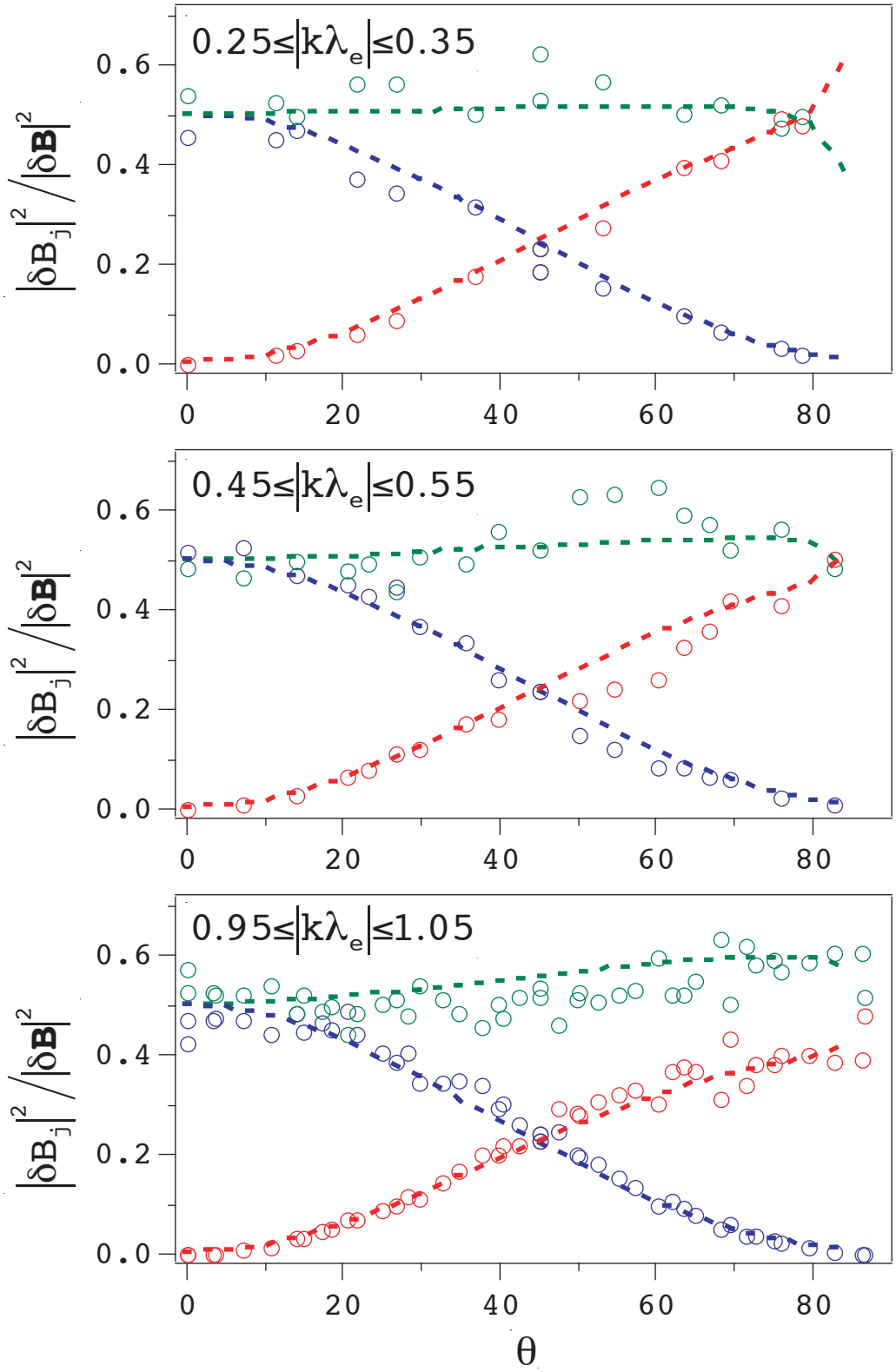
0.25≤|kλe|≤0.35
0.45≤|kλe|≤0.55
0.95≤|kλe|≤1.05
|δBj|2 / |δB|2
0.0
0.2
0.4
0.6
0
20
40
60
80
θ

Figure 4

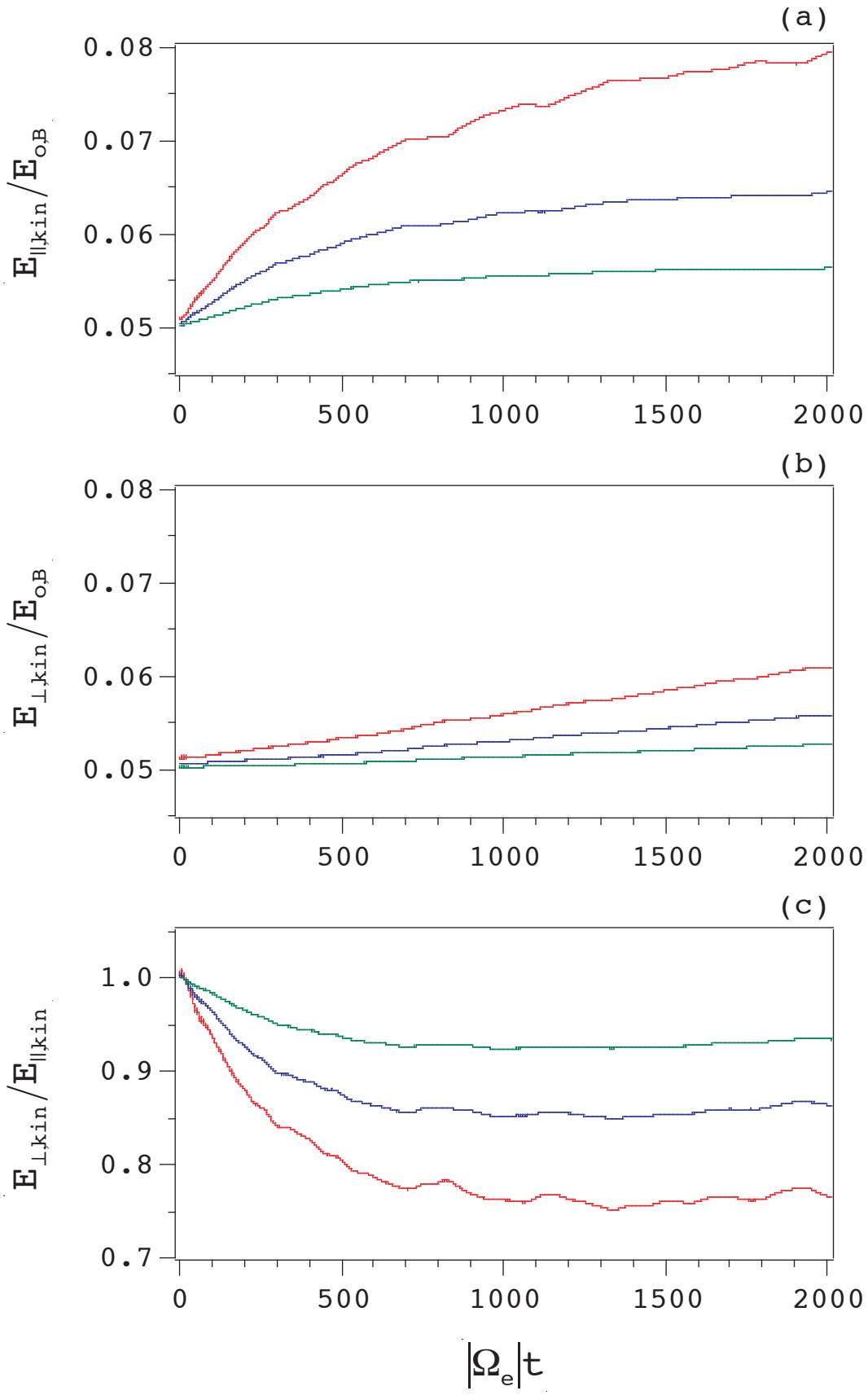
(a)
0.08
0.07
0.06
0.05
$E_{\|,kin}/E_{o,B}$
0
500
1000
1500
2000
(b)
0.08
0.07
0.06
0.05
$E_{\perp,kin}/E_{o,B}$
0
500
1000
1500
2000
(c)
1.0
0.9
0.8
0.7
$E_{\perp,kin}/E_{\|,kin}$
0
500
1000
1500
2000
$|\Omega_e|t$

Figure 5

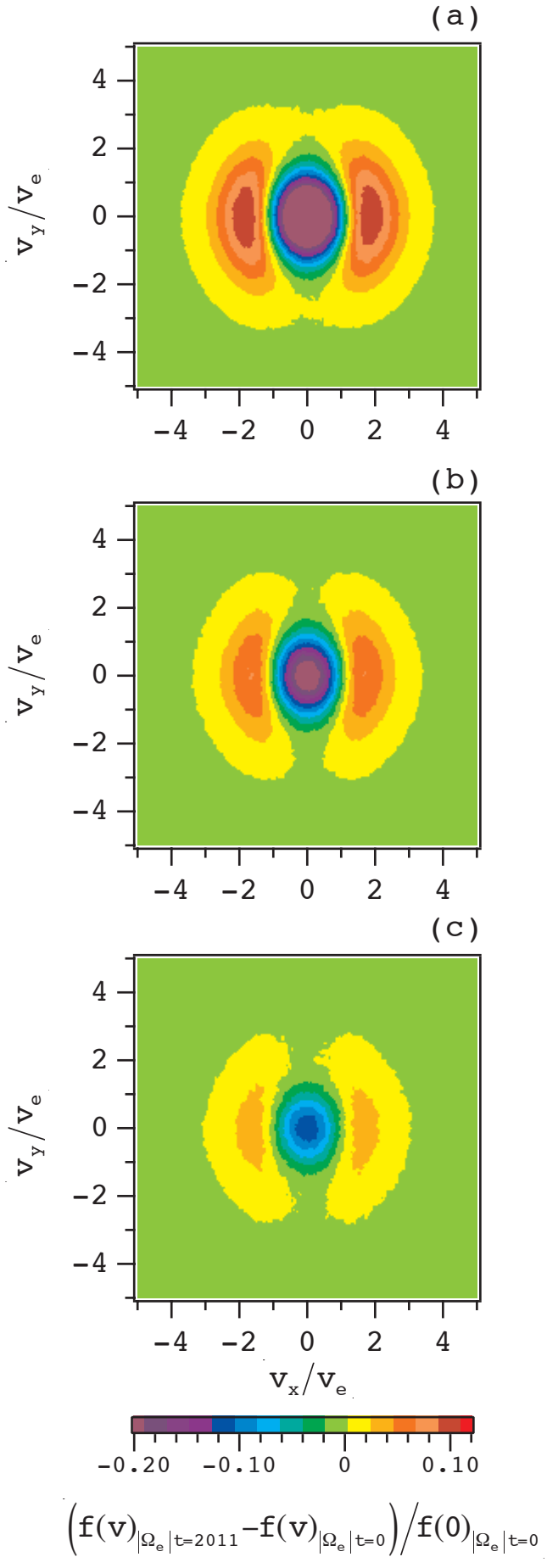
(a)
(b)
(c)
4
2
0
−2
−4
−4
−2
0
2
4
v_y/v_e
v_x/v_e
−0.20
−0.10
0
0.10
$\left(f(v)_{|\Omega_e|t=2011} - f(v)_{|\Omega_e|t=0}\right) / f(0)_{|\Omega_e|t=0}$

Figure 6

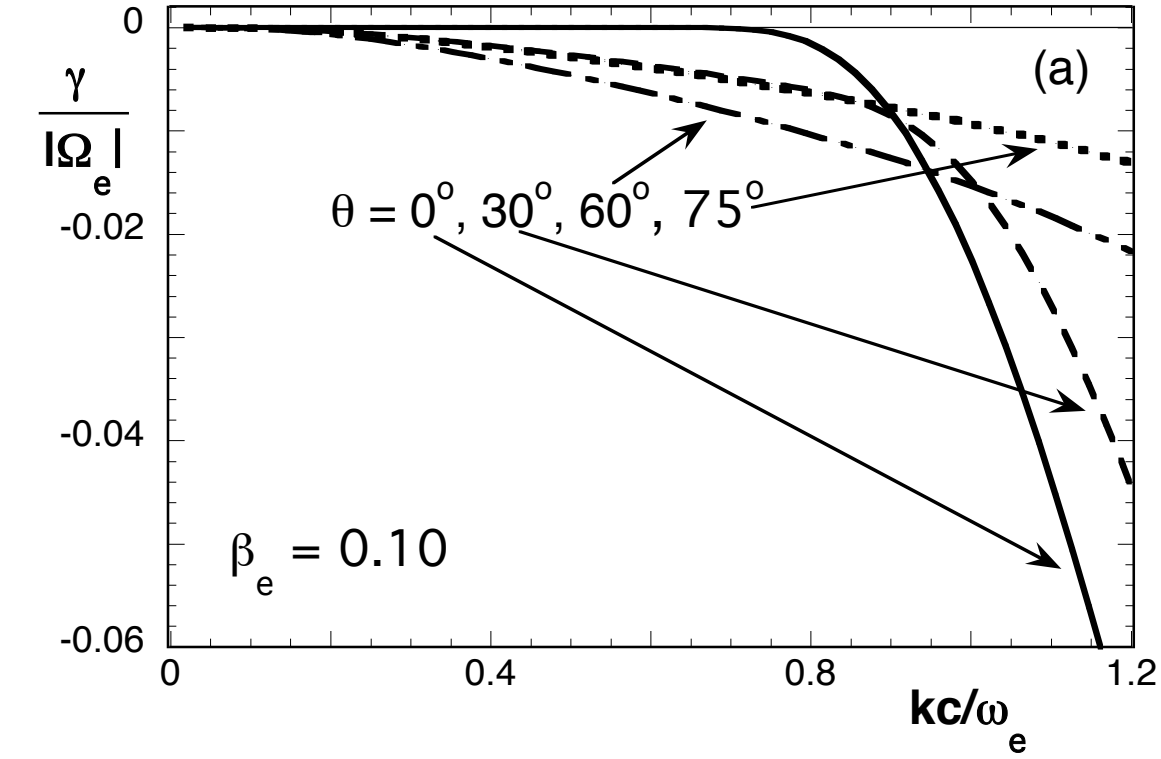
0
γ / |Ω_e|
-0.02
-0.04
-0.06
(a)
θ = 0°, 30°, 60°, 75°
β_e = 0.10
0
0.4
0.8
1.2
kc/ω_e

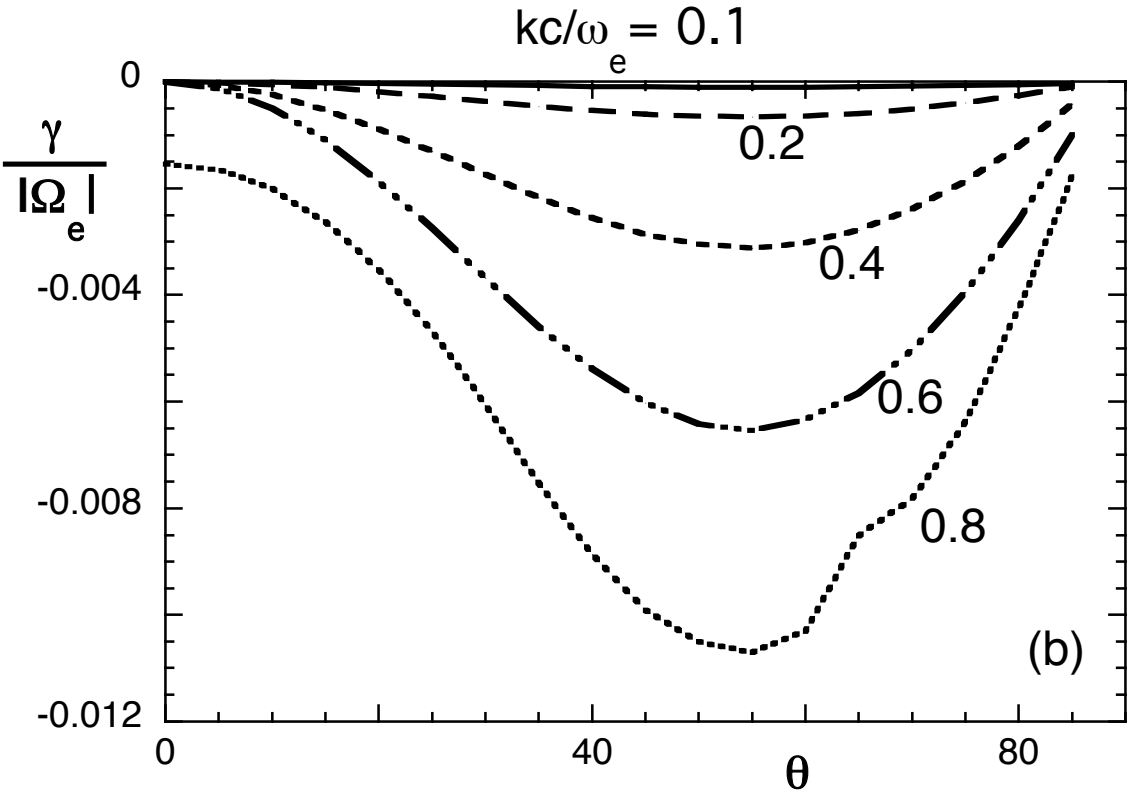
kc/ω_e = 0.1
0
γ / |Ω_e|
-0.004
-0.008
-0.012
0.2
0.4
0.6
0.8
(b)
0
40
80
θ

Figure 7